Full-length Article

Azithromycin preserves adult hippocampal neurogenesis and behavior in a mouse model of sepsis

Carla B. Rodríguez-Moreno [a,b], Héctor Cañeque-Rufo [c,d], Miguel Flor-García [a,b,e], Julia Terreros-Roncal [a,b,e], Elena P. Moreno-Jiménez [a,b,e], Noemí Pallas-Bazarra [f,g], Carlo Bressa [h], Mar Larrosa [i], Fabio Cafini [j,*], María Llorens-Martín [a,b,*]

[a] Department of Molecular Neuropathology, Centro de Biología Molecular "Severo Ochoa" (CBMSO), Spanish Research Council (CSIC)–Universidad Autónoma de Madrid (UAM), Madrid, Spain
[b] Center for Networked Biomedical Research on Neurodegenerative Diseases (CIBERNED), Madrid, Spain
[c] Department of Chemistry and Biochemistry, School of Pharmacy, Universidad San Pablo-CEU, CEU Universities, Urbanización Montepríncipe, 28660 Boadilla del Monte, Spain
[d] Department of Health and Pharmaceutical Sciences, School of Pharmacy, Universidad San Pablo-CEU, CEU Universities, Urbanización Montepríncipe, 28660 Boadilla del Monte, Spain
[e] Department of Molecular Biology, Faculty of Sciences, Universidad Autónoma de Madrid, Madrid, Spain
[f] Centre for Developmental Neurobiology, Institute of Psychiatry, Psychology and Neuroscience, King's College London, London SE1 1UL, UK
[g] MRC Centre for Neurodevelopmental Disorders, King's College London, London SE1 1UL, UK
[h] Facultad de Ciencias Experimentales, Universidad Francisco de Vitoria, Ctra. Pozuelo-Majadahonda Km 1,800, 28223, Pozuelo de Alarcón, Madrid
[i] Department of Food Science and Nutrition, Faculty of Pharmacy, Universidad Complutense de Madrid, 28040 Madrid, Spain
[j] Faculty of Biomedical and Health Sciences, Universidad Europea de Madrid, Madrid, Spain

ARTICLE INFO

ABSTRACT

The mammalian hippocampus can generate new neurons throughout life. Known as adult hippocampal neurogenesis (AHN), this process participates in learning, memory, mood regulation, and forgetting. The continuous incorporation of new neurons enhances the plasticity of the hippocampus and contributes to the cognitive reserve in aged individuals. However, the integrity of AHN is targeted by numerous pathological conditions, including neurodegenerative diseases and sustained inflammation. In this regard, the latter causes cognitive decline, mood alterations, and multiple AHN impairments. In fact, the systemic administration of Lipopolysaccharide (LPS) from *E. coli* to mice (a model of sepsis) triggers depression-like behavior, impairs pattern separation, and decreases the survival, maturation, and synaptic integration of adult-born hippocampal dentate granule cells. Here we tested the capacity of the macrolide antibiotic azithromycin to neutralize the deleterious consequences of LPS administration in female C57BL6J mice. This antibiotic exerted potent neuroprotective effects. It reversed the increased immobility time during the Porsolt test, hippocampal secretion of pro-inflammatory cytokines, and AHN impairments. Moreover, azithromycin promoted the synaptic integration of adult-born neurons and functionally remodeled the gut microbiome. Therefore, our data point to azithromycin as a clinically relevant drug with the putative capacity to ameliorate the negative consequences of chronic inflammation by modulating AHN and hippocampal-related behaviors.

1. Introduction

The hippocampus participates in the regulation of memory and emotions. This structure continues to generate new neurons postnatally (Altman, 1963; Eriksson et al., 1998) through adult hippocampal neurogenesis (AHN). This process confers enhanced synaptic plasticity throughout life and results in the continuous incorporation of new dentate granule cells (DGCs) into the hippocampal circuitry. The

---

addition of new neurons participates in pattern separation, episodic memory, forgetting, and mood regulation (Akers et al., 2014; Hill et al., 2015; Sahay et al., 2011). Among other factors, stress (Gould et al., 1997) and inflammation (Monje et al., 2003) are potent negative regulators of AHN. Several mechanisms, including surges of glucocorticoids and pro-inflammatory cytokines, underlie stress- and inflammation-mediated AHN impairments (reviewed in (Lucassen et al., 2010)). Further complexity is introduced into the aforementioned regulatory loop by the gut microbiome, a key modulator of AHN (Grabrucker et al., 2023; Guzzetta et al., 2022; Ogbonnaya et al., 2015) that is also remodeled under stress and pro-inflammatory conditions (Sherwin et al., 2016).

Given the potential relevance of neuroinflammation as a clinical target to treat neurodegenerative diseases (Morris et al., 2020), the permanent cognitive impairments reported in a considerable number of patients after sepsis (Browne et al., 2022), as well as the key role played by adult neurogenesis in hippocampal-dependent functions (Hill et al., 2015; Sahay et al., 2011), there is an urgent need to identify novel drugs that can efficiently counteract the negative consequences of systemic inflammation. Here we studied the capacity of azithromycin, a macrolide antibiotic with enhanced tissue penetration and anti-inflammatory properties, to neutralize the deleterious effects caused by the systemic administration of Lipopolysaccharide (LPS) from *E. coli* to mice—a mouse model of sepsis characterized by depression-like behavior (Yirmiya, 1996) and AHN impairments (Llorens-Martin et al., 2014). Azithromycin is used to treat respiratory tract infections caused by bacteria. However, its antiviral properties are also beneficial for patients with COVID-19 (Venditto et al., 2021) and Zika (Retallack et al., 2016) infections. Some of the anti-inflammatory potential of azithromycin appears to be mediated by its capacity to polarize macrophages and neutrophils toward protective phenotypes (Amantea et al., 2016; Easton, 2013; Murphy et al., 2008; Petrelli et al., 2016) and to modulate the secretion of pro- and anti-inflammatory cytokines (Haydar et al., 2019). Although this antibiotic is widely used as an immunomodulatory drug in patients with chronic inflammatory diseases (Amantea and Bagetta, 2016; Equi et al., 2002; Kang et al., 2016; Kitsiouli et al., 2015; Wiselka et al., 1996), the cellular and molecular mechanisms underlying its action have not been fully characterized to date. To the best of our knowledge, this is the first study to assess the putative effects of azithromycin on AHN. We interrogated the cellular mechanisms underpinning the neuroprotective capacity of azithromycin to reverse the behavioral and AHN impairments caused by LPS, focusing on the hippocampal inflammatory milieu, the functional integration of newly generated DGCs, and the gut microbiome. To this end, we used distinct retroviruses, behavioral analyses, cytokine arrays, as well as next-generation sequencing (NGS) and metagenome functional prediction analyses related to the fecal microbiome.

2. Material and methods

2.1. Experimental design

To avoid the negative impact of hierarchy/ dominance relationships between male mice on AHN (Kozorovitskiy and Gould, 2004), only female mice were used in this study. Animals received a subcutaneous osmotic pump to achieve continuous delivery of LPS (n = 40) or PBS (n = 40). Half the mice in each group received either oral azithromycin (n = 40) or drinking water alone (n = 40) during the same period. Thus, 4 experimental groups were included in this study: PW (PBS/Water), PA (PBS/Azithromycin), LW (LPS/Water), and LA (LPS/Azithromycin).

A first sub-group of 28 x 9-week-old female C57BL6J Ola Hsd mice (7 PW, 7 PA, 7 LW, and 7 LA) was used to analyze the fecal microbiome, brain cytokine expression, and behavior (Fig. 1A). A second group of 20 x 9-week-old female C57BL6J Ola Hsd mice (5 PW, 5 PA, 5 LW, and 5 LA) was used to study AHN and microglia (Fig. 2A). These animals were treated with LPS, azithromycin, both, or their respective vehicles for 14

days. Twenty-four hours before sacrifice, the mice received an i.p. injection of 5-Iodo-2´-deoxyuridine (IdU). To assess neuronal maturation and synaptic integration respectively, two groups of 16 x 7-week-old mice, which differed in post-injection survival time (either 14 days (4 PW, 4 PA, 4 LW, and 4 LA) (Fig. 3A) or eight weeks (4 PW, 4 PA, 4 LW, and 4 LA) (Fig. 4A)), were also included. These animals received a stereotaxic injection of GFP- (14 days) or Synaptophysin (Syn)-GFP- (8 weeks) encoding retroviruses and were sacrificed after the aforementioned post-injection intervals.

2.2. Animals

Female C57BL6J-OlaHsd mice aged between 6 and 8 weeks were obtained from Envigo Laboratories. They were subjected to a one-week habituation period before the experiments began. Animals were housed in a specific pathogen-free colony facility at the *Centro de Biología Molecular Severo Ochoa* (CBMSO) following European Community Guidelines (directive 86/609/EEC) and handled following European and local animal care protocols. Three to five mice were housed per cage. Animal experiments were approved by the CBMSO (AEEC-CBMSO-23/172) and the National (PROEX 205/15 and PROEX 185.4/20) Ethics Committees.

2.3. Administration of lipopolysaccharide from E. coli (LPS)

LPS was chronically administered subcutaneously for 2 or 8 weeks via Alzet® osmotic pumps (#1002# or #1004# models respectively, 0.11 μl/h) (Durect Corporation, Cupertino, California). To achieve a continuous LPS delivery of 300 μg/kg/day, pumps were filled with a solution of LPS (Sigma, from *Escherichia coli* 055:B5, St. Louis, MO) diluted in 0.1 M saline phosphate buffer (PBS). To administer LPS for 8 weeks, the pumps were replaced by new ones 4 weeks after the beginning of the treatment. Control mice carried PBS-containing osmotic pumps and were subjected to the same experimental manipulations as LPS-treated mice. To implant the pumps, a subcutaneous incision was made on the back of the animal under inhaled isoflurane full anesthesia. The skin was separated to create a space where the pumps were implanted. Wounds were closed with 2 to 3 staples. The pumps were implanted 12 h after the start of azithromycin administration and 12 h before stereotaxic surgery.

2.4. Treatment with azithromycin

Animals received 0.625 mg/ml of azithromycin (Zithromax®; Pfizer) in drinking water (or water alone) for either 2 or 8 weeks. On the basis of the average water consumption and body weight of the mice, the dose of azithromycin was calculated to be 25 mg/kg/day (Vallee et al., 1992).

2.5. Retroviral stock preparation

We used two replication-incompetent retroviruses, which allowed the labeling of cells undergoing division at the time of surgery (Kelsch et al., 2008). These retroviruses encode for either green fluorescent protein (GFP) (CAG-GFP) (Zhao et al., 2006) or synaptophysin (Syn) fused to GFP (Syn-GFP) (Kelsch et al., 2008; Kelsch et al., 2009). GFP-expressing retroviruses allowed the analysis of newborn DGC morphology at the initial stages of maturation (2 weeks post-injection) while Syn-GFP retroviruses were also used to study morphology and the active zone of the mossy fiber terminals (MFTs) of 8-week-old newborn DGCs, a parameter that reflects their efferent connectivity (Kelsch et al., 2008; Kelsch et al., 2010). Anti-GFP immunohistochemistry (IHC) enhanced the visualization of the intracellular trafficking of GFP, thereby revealing the whole morphology of the cells, including their dendrites, axon, and MFTs (Kelsch et al., 2008; Llorens-Martin et al., 2013). The plasmids used to produce the GFP-expressing retroviruses were a generous gift from Prof. Fred H. Gage (Salk Institute), while those used to produce the Syn-GFP retrovirus were kindly
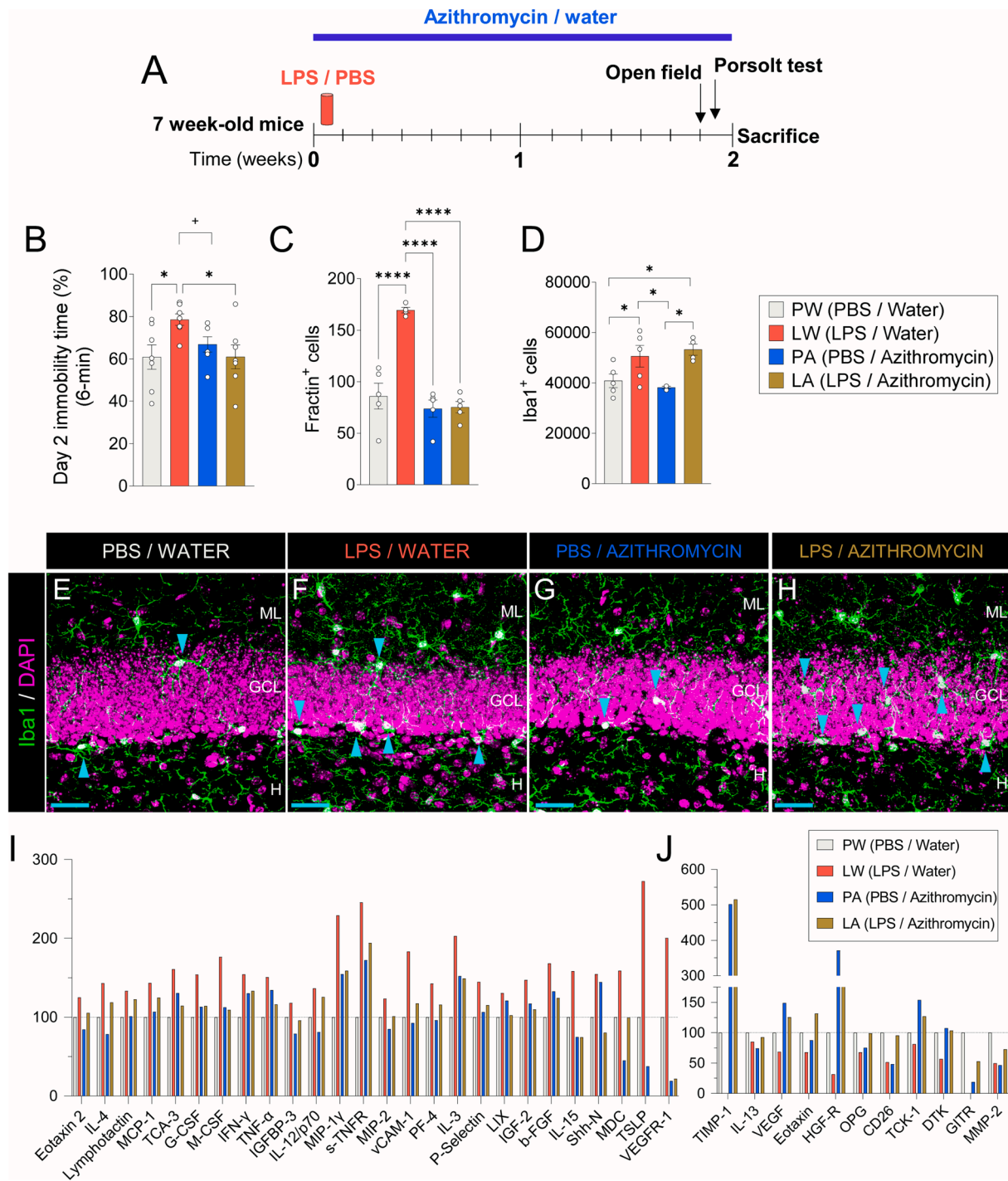
Fig. 1. Effects of lipopolysaccharide (LPS) and azithromycin administration on mouse performance in the Porsolt test, neuroinflammation, and microglial cells. **A:** Experimental design. **B:** Time immobile during the Porsolt test. **C:** Number of Fractin+ apoptotic cells. **D:** Number of Iba1+ cells in the dentate gyrus (DG). **E – H:** Representative images showing Iba1+ microglia in the DG. **I – J:** Cytokine levels in the hippocampus. The expression of Eotaxin-2, Interleukin-4 (IL-4), Lymphotactin, Monocyte Chemoattractant Protein-1 (MCP-1), TCA-3, Granulocyte colony-stimulating factor (G-CSF), Monocyte colony-stimulating factor (M−CSF), γ-Interferon (IFN-γ), Tumor necrosis factor-α (TNF-α), Insulin-like Growth Factor Binding Protein-3 (IGFBP-3), Interleukin-12/p70 (IL-12/p70), Macrophage inflammatory protein 1γ (MIP-1γ), soluble-TNF receptor (s-TNFR), Macrophage inflammatory protein 2 (MIP-2), Vascular cell adhesion protein 1 (vCAM-1), Platelet factor 4 (PF4), Interleukin-3 (IL-3), P-Selectin, Lipopolysaccharide-induced CXC chemokine (LIX), Insulin-like Growth Factor 2 (IGF-2), basic fibroblast growth factor (b-FGF), Interleukin-15 (IL-15), Sonic Hedgehog N-Terminus Protein (Shh-N), Macrophage-derived chemokine (MDC), Thymic stromal lymphopoietin (TSLP), and Vascular endothelial growth factor receptor 1 (VEGFR-1) was upregulated in LPS-treated mice and normalized after azithromycin administration (**I**). Conversely, the expression of Tissue inhibitor of metalloproteinases 1 (TIMP-1), Interleukin-13 (IL-13), Vascular endothelial growth factor (VEGF), Eotaxin, Hepatocyte growth factor receptor (HGF-R), Osteoprotegerin (OPG), CD26, cytokine-stimulated T cells 1 (TCK-1), Developmental receptor tyrosine kinase (DTK), Glucocorticoid-induced TNF-related receptor (GITR), and Matrix metalloproteinase-2 (MMP-2) was upregulated in azithromycin-treated mice (**J**). The results relative to the full array of cytokines determined are shown in Supplementary Fig. S2. In **E – H**, Z-projection images are shown. Graphs represent mean values ± SEM. ML: Molecular layer. GCL: Granule cell layer. H: Hilus. Blue scale bar: 50 µm. Blue triangles: Iba1+ microglia. * $0.05 > p \geq 0.01$; **** $p < 0.0001$.
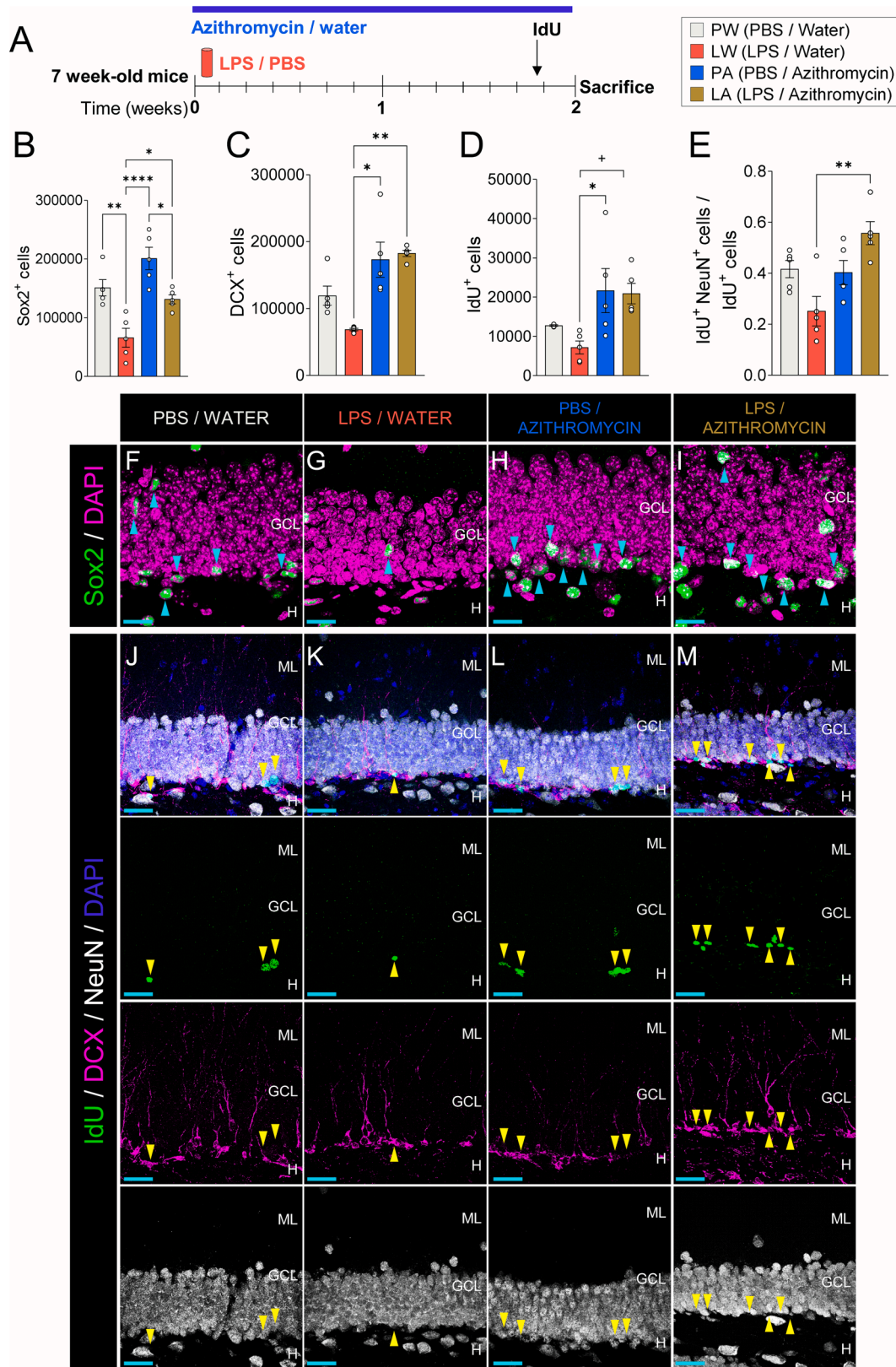
Fig. 2. Effects of 2 weeks of lipopolysaccharide (LPS) and azithromycin administration on the hippocampus. A: Experimental design. **B:** Number of SRY (sex determining region Y)-box 2 (Sox2)$^+$ cells. **C:** Number of Doublecortin (DCX)$^+$ cells. **D:** Number of 5-Iodo-2′-deoxyuridine (IdU)$^+$ cells. **E:** Number of IdU$^+$ Neuronal nuclei (NeuN)$^+$ cells out of the total number of IdU$^+$ cells. **F – I:** Representative images of Sox2$^+$ cells in the dentate gyrus (DG). **J – M:** Representative images of IdU$^+$, DCX$^+$, and NeuN$^+$ cells. In **F – M**, Z-projection images are shown. Graphs represent mean values ± SEM. ML: Molecular layer. GCL: Granule cell layer. H: Hilus. Blue scale bar: 25 μm. Blue triangles: Sox2$^+$ cells. Yellow triangles: IdU$^+$ cells. + 0.09 > p ≥ 0.05; * 0.05 > p ≥ 0.01; ** 0.01 > p ≥ 0.001; and **** p < 0.0001. (For interpretation of the references to colour in this figure legend, the reader is referred to the web version of this article.)
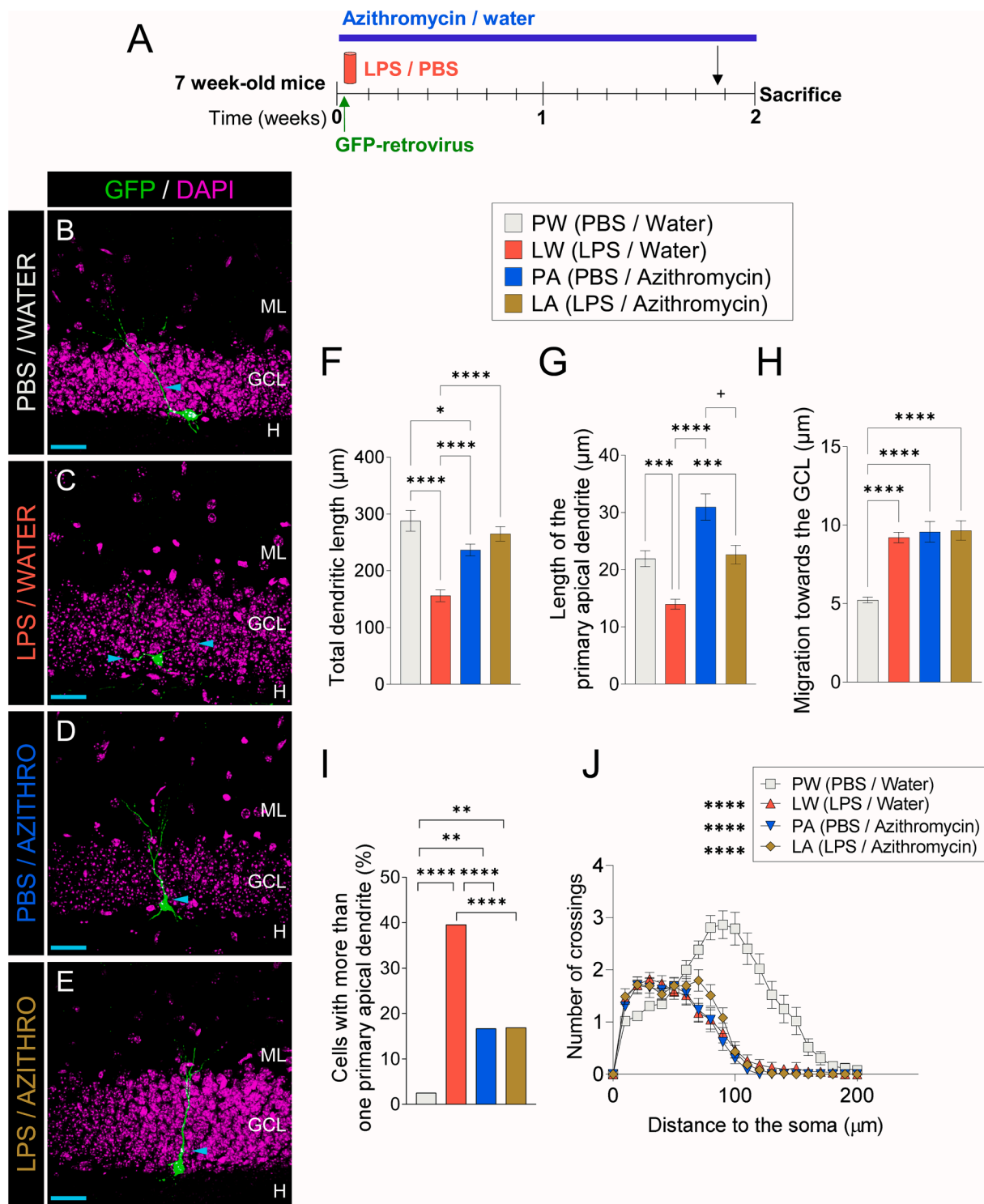
Fig. 3. Effects of 2 weeks of lipopolysaccharide (LPS) and azithromycin administration on the early maturation of newborn dentate granule cells (DGCs). **A:** Experimental design. **B – E:** Representative images of 2-week-old newborn DGCs transduced with a GFP-encoding retrovirus. **F:** Total dendritic length. **G:** Length of the primary apical dendrites. **H:** Migration towards the granule cell layer (GCL). **I:** Percentage of newborn DGCs with more than one single primary apical dendrite. **J:** Sholl's analysis. In **B – E**, Z-projection images are shown. Graphs represent mean values ± SEM. ML: Molecular layer. GCL: Granule cell layer. H: Hilus. Blue scale bar: 50 μm. Blue triangles: Primary apical dendrites. $+$ $0.09 > p \geq 0.05$; * $0.05 > p \geq 0.01$; ** $0.01 > p \geq 0.001$; *** $0.001 > p \geq 0.0001$; and **** $p < 0.0001$. (For interpretation of the references to colour in this figure legend, the reader is referred to the web version of this article.)

provided by Prof. Carlos Lois (Caltech). Retroviral stocks were concentrated to working titers of $1 \times 10^7 - 1 \times 10^8$ pfu/ml by ultracentrifugation (Zhao et al., 2006).

2.6. Stereotaxic surgery

Seven-week-old mice were anesthetized with isoflurane and placed in a stereotaxic frame. Viruses were injected into the dentate gyrus (DG) at the following coordinates (mm) relative to bregma in the
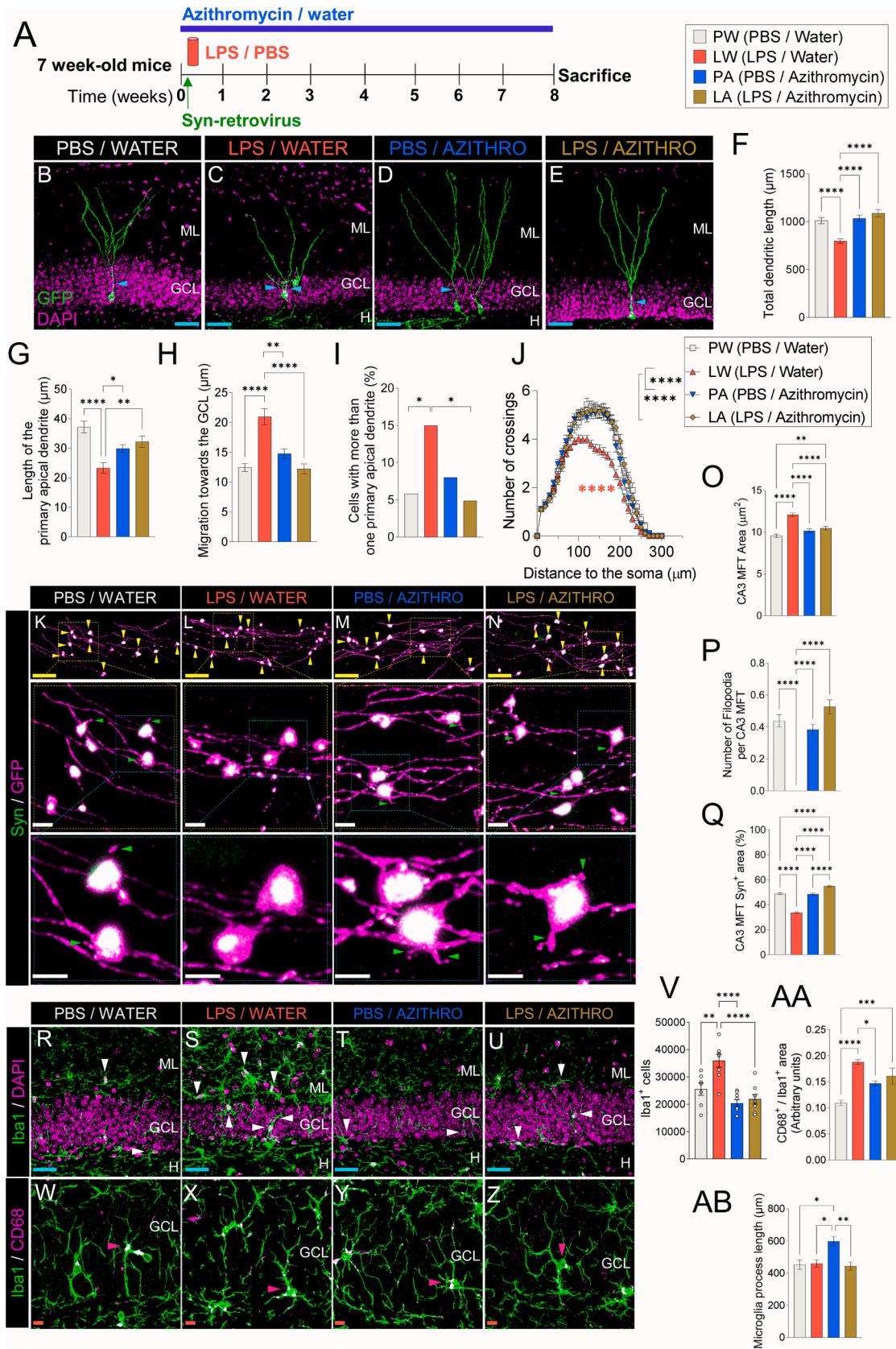
(caption on next page)

Fig. 4. Effects of 8 weeks of lipopolysaccharide (LPS) and azithromycin administration on the late maturation of newborn dentate granule cells (DGCs). **A:** Experimental design. **B – E:** Representative images of 8-week-old newborn DGCs transduced with a Synaptophysin (Syn)-GFP encoding retrovirus. **F:** Total dendritic length. **G:** Length of the primary apical dendrite. **H:** Migration towards the granule cell layer (GCL). **I:** Percentage of newborn DGCs with more than one single primary apical dendrite. **J:** Sholl's analysis. **K-N:** Representative images of Synaptophysin (Syn)[+] clusters in the mossy fiber terminals (MFTs) of 8-week-old newborn DGCs. **O:** Area of MFTs in the CA3 region. **P:** Number of filopodia per MFT in the CA3 region. **Q:** Percentage of Syn[+] area in MFTs of the CA3 region. **R - U:** Representative images showing Iba1^{+} microglia. **V:** Number of Iba1^{+} cells. **W-Z:** Representative high-power images showing CD68 expression in Iba1^{+} microglia. **AA** Iba1^{+} area that is CD68^{+}. **AB:** Total length of microglia processes. In **B – E**, **K – N**, **R-U**, and **W-Z**, Z-projection images are shown. Graphs represent mean values ± SEM. ML: Molecular layer. GCL: Granule cell layer. H: Hilus. Blue scale bar: 50 μm. Orange scale bar: 10 μm. Yellow scale bar: 7 μm. White scale bar: 1 μm. Blue triangles: Primary apical dendrite. Yellow triangles: MFTs. Green triangles: Filopodia. White triangles: Iba1^{+} microglia. Pink triangles: CD68^{+} clusters. * $0.05 > p \geq 0.01$; ** $0.01 > p \geq 0.001$; *** $0.001 > p \geq 0.0001$; and **** $p < 0.0001$. Red asterisks indicate statistically significant differences between the LW and PW groups. (For interpretation of the references to colour in this figure legend, the reader is referred to the web version of this article.)

---

anteroposterior, mediolateral, and dorsoventral axes: [-2.0, ±1.4, 2.2]. Next, 2 μl of virus was infused at a rate of 0.2 μl/min via a glass micropipette. To avoid any suction effect, micropipettes were kept in place at the site of injection for an additional 5 min before being slowly removed. Three days prior to stereotaxic injections, a running wheel was included in the cage to enhance stem cell proliferation.

2.7. Administration of 5-Iodo-2'-deoxyuridine (IdU)

IdU (Sigma-Aldrich, St. Louis, MO) was injected i.p. at a concentration of 57.65 mg/Kg, diluted in 1X PBS containing two drops of 5 N NaOH per 10–15 mL PBS to increase IdU solubility. This dose was based on equimolar doses of 50 mg/Kg BrdU (Lugert et al., 2010; Llorens-Martin et al., 2010). To label dividing cells, 24 h before sacrifice, IdU was administered to animals not subjected to behavioral testing (Fig. 2A).

2.8. Open field test

Animals were exposed to a square (45 × 45 cm), constantly illuminated, open-field methacrylate arena in a single 10-min trial. Animal performance was recorded with a video camera and subsequently analyzed. The total distance moved, average speed, and total time mobile were determined as previously described (Llorens-Martin et al., 2014), and are shown in Supplementary Fig. S1J–L.

2.9. Forced swimming test (Porsolt test)

Animals were placed in a 12-cm-diameter and 29-cm-tall cylinder filled with water at 23 °C for 6 min on 2 consecutive days. Behavior was digitally recorded and manually assigned to a category, namely immobility, swimming, or climbing, following Detke et al. (Detke et al., 1995). The time spent immobile, swimming, and climbing during the whole test (6 min, Fig. 1 and Supplementary Fig. S1A–C), and the last 5 (Supplementary Fig. S1D–F) and 4 (Supplementary Fig. S1G–I) min of the second day of testing are reported, as previously described (Llorens-Martin et al., 2016).

2.10. Sacrifice

Mice were fully anesthetized by an i.p. injection of pentobarbital (EutaLender, 60 mg/kg) and transcardially perfused with 0.9 % saline. Afterwards, those that received retrovirus injections were perfused with 4 % paraformaldehyde in 0.1 N phosphate buffer (PB), and brains were removed and post-fixed O/N in the same fixative at 4 °C. After being transcardially perfused with 0.9 % saline, the brains of mice subjected to biochemical and immunohistochemistry (IHC) determinations were removed and divided into two hemispheres. Right hemispheres were post-fixed O/N with 4 % paraformaldehyde in 0.1 N PB. Left hippocampi were rapidly dissected on ice and immediately frozen at −80 °C.

2.11. Immunohistochemistry

After fixation, brains were washed three times in 0.1 N PB. Coronal

50 μm-thick sections were obtained on a Leica VT1200S vibratome. For immunohistochemical analyses, series of brain slices were randomly made up of one section from every ninth. Slices were initially pre-incubated in 0.1 N PB with 1 % Triton X-100 (Sigma, #T8787#) and 1 % bovine serum albumin (BSA) (Panreac, #A13910100#) for 10 min. To detect the incorporation of IdU, sections were incubated in 2 N Hydrochloric acid (HCl) for 30 min at room temperature to denature DNA. Dual or triple IHC was then performed as described previously (Llorens-Martin et al., 2013), using the following primary antibodies: rabbit anti-GFP (Thermo Fisher Scientific Cat# A-11122, RRID:AB_221569; 1:1000); mouse anti-IdU (Becton Dickinson and Company Cat# 347580, RRID:AB_10015219; 1:500); rabbit anti-Fractin (Acris Antibodies GmbH Cat# AP08647SU-N, RRID:AB_1975531; 1:500); guinea pig anti-Doublecortin (DCX) (Synaptic systems Cat# 326004, RRID: AB_2620068; 1:500); *Wisteria floribunda* agglutinin (Lectin) (Sigma Cat# L1516, RRID: AB_2620171, 1:500); chicken anti-Iba1 (Synaptic systems Cat# 234006, RRID:AB_2619949; 1:1000); rabbit anti-phospho Histone3 (PH3) (Millipore Cat# 06–570, RRID: AB_310177, 1:250); goat anti-Sox2 (R&D Systems Cat# AF2018, RRID: AB_355110, 1:500); rabbit anti-NeuN (Millipore Cat# ABN78, RRID: AB_10807945, 1:1000); and rat anti-CD68 (Abcam Cat# ab53444, RRID: AB_869007, 1:500). Sections were incubated with primary antibodies for 2 days at 4 °C. To detect the binding of primary antibodies, sections were incubated with the following secondary antibodies for 24 h at 4 °C: Alexa-594 donkey anti-mouse (Molecular Probes Cat# A-21203, RRID:AB_141633; 1:1000); Alexa-555 donkey anti-rabbit (Molecular Probes Cat# A-31572, RRID:AB_162543; 1:1000); Alexa-488 donkey anti-rabbit (Molecular Probes Cat# A-21206, RRID:AB_141708; 1:1000); Alexa-555 donkey anti-rat (Molecular Probes Cat# A-21434, RRID:AB_141733; 1:1000); and Alexa-555 goat anti-guinea pig (Molecular Probes Cat# A-21435, RRID:AB_2535856; 1:1000). All the sections were counter-stained for 10 min with DAPI (Merck, 1:5000) to label cell nuclei. Finally, they were mounted on gelatin-coated glass slides. A non-commercial anti-fade mounting medium (33 % glycerol and 7.5 % Mowiol, prepared in 0.2 M Tris-HCl, pH 8.5) was used to embed the sections.

2.12. Nissl staining and volume estimation

A randomly chosen series of sections was mounted on gelatin-coated glass slides and air-dried to perform Nissl staining and to calculate the volume of the granule cell layer (GCL) and the area of the subgranular zone (SGZ). Slides were immersed in a toluidine blue solution for 8 min and rinsed for 10 sec in distilled water. Next, subsequent 2-min incubations in 70 %, 96 %, 100 % (x2) ethanol were performed. Finally, slides were immersed in xylene and mounted with DePex (Serva Electrophoresis GmbH, #18243.01#). Bilateral images of the whole DG were acquired under a 2.5X objective in an Axioskop2 plus (Zeiss) vertical microscope coupled to a DMC6200 (Leica) camera. The volume of the GCL was calculated using the Cavalieri method (Pakkenberg and Gundersen, 1988). Briefly, the area of the GCL was manually drawn in *Fiji* (ImageJ,v. 1.50e, NIH, Bethesda, MD, USA, https://rsb.info.nih.gov/ij). The area of the GCL of all the sections included in the series was multiplied by the distance between two consecutive sections (400 μm) to

calculate the total volume of this layer. The area of the SGZ was calculated using a modified version of the Cavalieri method (Llorens-Martin et al., 2006). To this end, the length of the SGZ was measured in each section using *Fiji*. The length of the SGZ of all the sections included in the series was multiplied by the distance between two consecutive sections (400 μm) to calculate the area of this zone, as previously described (Llorens-Martin et al., 2006).

2.13. Cell counts

Fractin$^+$ and PH3$^+$ cells were counted on independent series of sections under an Axioskop2 plus (Zeiss) vertical microscope coupled to a DMC6200 (Leica) camera using the optical dissector method. Briefly, the density of cells per section (number of cells/mm^3) was calculated by dividing the number of cells counted by the reference volume of that section. The average cell density of the sections included in the series was multiplied by the GCL volume to calculate the total number of cells per mouse. The number of Sox2$^+$, IdU$^+$, Iba1$^+$, and DCX$^+$ cells was estimated using the physical dissector method coupled to a confocal microscope (Llorens-Martin et al., 2006). Briefly, 10 stacks of images per mouse were acquired to estimate the total number of IdU$^+$ cells (40X oil-immersion objective, z-interval: 1 μm, 0,8 zoom), and 5 stacks of images per mouse were acquired to estimate the total number of DCX$^+$, Iba1$^+$, and Sox2$^+$ (63X oil-immersion objective, Z–interval: 1 μm, 0.8 zoom) cells under an LSM800 inverted Zeiss confocal microscope. The number of IdU$^+$ and Sox2$^+$ cells in each stack was divided by the volume of the GCL, whereas that of DCX$^+$ cells was divided by the area of the SGZ. To obtain the total number of cells per mouse, the average cell density was multiplied by either the GCL volume (Sox2$^+$, Iba1$^+$, and IdU$^+$ cells) or the SGZ area (DCX$^+$ cells), following a previously described method (Llorens-Martin et al., 2006).

2.14. Colocalization analyses

The percentage of IdU$^+$ cells that were positive for NeuN was determined by analyzing the expression of the latter marker in this cell population per mouse. To this end, confocal stacks of images (40X oil-immersion objective, z-interval: 1 μm, 0.8 zoom, XY dimensions: 79.38 μm) were obtained. To address microglial activation, we measured CD68 expression in Iba1$^+$ cells. Briefly, 5 stacks of 20 images were obtained per mouse under an LSM800 Zeiss confocal microscope (40x Oil immersion objective, Z-axis interval: 1 μm, 0.8 zoom, XY dimensions: 79.38 μm). Three-channel images were acquired (DAPI, CD68, and Iba1). For each image, a fixed value threshold was applied to the Iba1 channel, and then the threshold image was converted into a Selection. A mean filter (2 pixels) was applied to exclude small precipitates of the secondary antibody. The Selection was then loaded onto the CD68 channel. Selections were inverted in both channels, and the exterior of the cells was filled with black paint. The resulting images were then processed with the *Just Another Colocalization Plugin (JACoP)* in ImageJ, as previously described (Llorens-Martin et al., 2016). The percentage of colocalization between the two channels (Iba1$^+$ area that was CD68$^+$ (Mander's coefficient M1)) was calculated.

2.15. Analysis of fluorescence intensity

Lectin staining was analyzed in the molecular layer (ML) and the GCL on confocal microscopy images obtained from the sections comprising one series. Four high magnification images per region were randomly obtained per animal under an A1R$^+$ Nikon confocal microscope (63X oil immersion objective, XY dimensions: 60.13 μm). In each sub-region, an invariant threshold for fluorescence intensity was established to analyze images. A region of interest (ROI) of invariant size (558.009 μm^2) was placed in two regions of the image, where the intensity of fluorescence was measured using ImageJ software (ImageJ,v. 1.33, NIH, https://rsb.info.nih.gov/ij).

2.16. Morphometric analysis of adult-born dentate granule cells and microglia

At least 50 randomly selected adult-born DGCs and 20 Iba1$^+$ microglia from each experimental condition were reconstructed in an LSM710 Zeiss confocal microscope (2-week-old newborn DGCs and Iba1$^+$ microglia: 40X oil immersion objective; 8-week-old newborn DGCs: 25X oil objective). Confocal stacks of images were obtained (2-week-old newborn DGCs and Iba1$^+$ microglia: XY dimensions: 212.55 μm; Z-axis interval: 2 μm; 8-week-old newborn DGCs: XY dimensions: 377.86 μm; Z-axis interval: 2 μm), and Z-projections were analyzed to determine the total length of dendritic/processes and branching (Shol's analysis). All cells were traced using the *NeuronJ* plugin for *Fiji*. Sholl's analysis was performed using the plugin *ShollAnalysis* for *Fiji*. (Llorens-Martin et al., 2013; Pallas-Bazarra et al., 2017). To measure adult-born DGC migration into the GCL, a perpendicular line connecting the hilar boundary and the center of the adult-born DGC nucleus was traced manually, and this distance was measured using *Fiji*. The percentage of cells with several primary apical dendrites and the length of the primary apical dendrite were calculated as previously described (Llorens-Martin et al., 2013; Pallas-Bazarra et al., 2016).

2.17. Analysis of mossy fiber terminals (MFTs) and filopodia

Retroviruses encoding synaptophysin (Syn)-GFP allowed the visualization of presynaptic active zones (Syn$^+$ clusters) (green channel, nude fluorescence of the retrovirus), whereas the use of a red secondary antibody coupled to an anti-GFP primary antibody enhanced the visualization of the intracellular trafficking of the free protein (red channel), thereby allowing visualization of the whole MFT (Kelsch et al., 2010). Images of the CA3 region were acquired under an LSM800 inverted Zeiss confocal microscope (63X oil-immersion objective, Z–interval: 1 μm, XY dimensions: 34.95 μm). Z–projection images were obtained, and the area of each MFT was measured by manually drawing these structures in *Fiji*. The number of filopodia per MFT was counted manually on Z-projection images. MFT and filopodia were identified on the basis of the following previously defined criteria: (1) the diameter of the MFT is more than threefold greater than the diameter of the axon; (2) the MFT is connected to the axon on at least one end; and (3) the MFT is relatively isolated from other MFTs for accuracy of tracing (Pallas-Bazarra et al., 2016; Toni et al., 2008). To measure the area of Syn$^+$ clusters in the MFTs, a fixed value threshold was first applied to the green (Syn) channel of the Z–projection images. The percentage of area occupied by the active area was calculated by dividing the area of the Syn$^+$ cluster by the total area of the MFT.

2.18. Analysis of cytokine expression levels

A longitudinally sectioned half of the left hippocampus was homogenized, and protein concentration was estimated using the BCA Protein Assay Kit (Pierce, Rockford, IL). For each experimental group, a pooled protein extract was prepared in a single tube. The total protein concentration was determined for each mouse to ensure an equal amount of protein corresponding to each animal in the prepared mixture. The mouse cytokine array (RayBio C-series Mouse Cytokine Antibody Array C1000; Ray Biotech Inc) consisted of 96 cytokine antibodies spotted onto a PVDF membrane. Incubations were performed following the manufacturer's instructions and as previously described (Llorens-Martin et al., 2016). For each spot, the net density of the gray level was measured in *Fiji*. For each experimental group, the relative expression of each cytokine was calculated. The mean is represented in the graphs.

2.19. Gut microbiome sequencing

One-to-two fecal samples per mouse were collected before sacrifice

in a sterile 2-ml tube and immediately frozen and stored at −80 °C. Bacterial DNA was obtained by using a QIAamp power fecal pro DNA kit from QIAGEN (#51804#) and following the manufacturer's instructions. Metagenome functional prediction analysis of the microbiota was performed using 16 s rRNA sequencing. A 459 bp fragment of the V3/V4 regions was amplified using the primer pair 341F/ 785R (5′-TCGT CGGC AGCG TCAG ATGT GTAT AAGA GACA GCCT ACGG GNGG CWGCA-G3′) / (5′-GTCT CGTG GGCT CGGA GATG TGTA TAAG AGAC AGAC AGGA CTAC HVGG GTAT CTAA TCC3′) (Klindworth et al., 2013). Library construction was performed following the Illumina 16S rRNA Cod 15,044,223 RevB protocol. The primers contained sequences added to the gene-specific sequences to make them compatible with the Illumina Nextera XT Index kit. The V3/V4 region of 16S rRNA was sequenced on Illumina Miseq with 2x250-2x300 length sequencing (paired-end) to obtain approximately 100,000 reads per sample.

2.20. Statistical analyses

Statistical analyses were performed using GraphPad v9.0 and SPSS25 software. The Kolmogorov–Smirnov test was used to check the normality of sample distribution. To compare more than two experimental groups, data following normal sample distribution were analyzed by either one-way or repeated-measures ANOVA tests with Fisher's LSD or Holm-Sidak multiple comparison post-hoc analyses. In cases in which normality could not be assumed, a Kruskal-Wallis test with Dunn's post-hoc analysis was applied. A two-way ANOVA was used to assess the effects of more than one variable. A Pearson X^2-test was used to compare qualitative variables. Correlations between cell numbers were analyzed using Pearson's correlation test. The detailed results of the statistical comparisons are included in Extended data 1.

For the gut microbiome sequencing analyses, data quality filtering was performed with QIIME2 v.2022.11 (Bolyen et al., 2019), and reads were assigned to Amplicon Sequence Variant (ASV) using DADA2 (Callahan et al., 2016). Taxonomic classification was obtained using classify-sklearn, a Scikit-Learn method (Pedregosa, 2011). The weighted classifier was constructed from Silva Database v. 138.1 including region V3-V4 and the weighted information was downloaded from readytowear (https://github.com/BenKaehler/readytowear, (Kaehler et al., 2019). Sequences that did not match any reference were discarded. The β-diversity microbiota index (Bray-Curtis) was examined by the Permutation-Based Analysis of Variance (PERMANOVA). Alpha diversity (Shannon) was studied using the Kruskal-Wallis test whereas Analysis of Compositions of Microbiomes with Bias Correction (ANCOM-BC) was used to identify bacterial taxa differentially represented between groups (Lin and Peddada, 2020). Diversity analyses were adjusted for multiple testing (q-values) using the Benjamini-Hochberg False Discovery Rate (FDR) (Benjamini and Hochberg, 1995), while ANCOM-BC analyses underwent correction via the Holm-Bonferroni method (Holm, 1979). Functional pathway abundance was predicted with Phylogenetic Investigation of Communities by Reconstruction of Unobserved States (PICRUSt2) (Douglas et al., 2020). A Linear discriminant analysis (LDA) coupled with effect size (LEfSe) was performed to identify functional pathways differentially represented between groups (Segata et al., 2011) (Supplementary Figs. S5–S10, and Extended data 2). Raw data corresponding to gut microbiome analyses were deposited at the NCBI Sequence Read Archive (SRA), ID number: PRJNA1020823.

In all the figures, asterisks refer to post-hoc analyses and show statistically significant differences between the two groups indicated. A 95 % confidence interval was used for statistical comparisons. The mean value and the standard error of the mean (±SEM) are shown in the graphs.

3. Results

3.1. Capacity of azithromycin to counteract the effects of LPS administration on behavior, the gut microbiome, and hippocampal inflammation

To assess the behavior of the animals in the distinct experimental groups, mice received osmotic pumps (filled with either LPS or PBS) and azithromycin or vehicle (drinking water) for 2 weeks before being subjected to the behavioral tests (Fig. 1A). In the open field test, no changes in the total distance moved ($F_{3, 24}$ = 0.261; p = 0.853; LPS: $F_{1, 24}$ = 0.1645; p = 0.689; azithromycin: $F_{1, 24}$ < 0.0001; p = 0.994; Interaction: $F_{1, 24}$ = 0.6175; p = 0.44) (Supplementary Fig. S1J), average speed ($F_{3, 24}$ = 0.537; p = 0.661; LPS: $F_{1, 24}$ = 0.0574; p = 0.813; azithromycin: $F_{1, 24}$ = 0.0141; p = 0.907; Interaction: $F_{1, 24}$ = 1.54; p = 0.227) (Supplementary Fig. S1K), or total time mobile ($F_{3, 24}$ = 0.170; p = 0.916; LPS: $F_{1, 24}$ = 0.0107; p = 0.919; azithromycin: $F_{1, 24}$ = 0.0904; p = 0.766; Interaction: $F_{1, 24}$ = 0.409; p = 0.529) (Supplementary Fig. S1L) were detected, thereby revealing no alterations in basal motor activity. Conversely, in the Porsolt test, the time spent immobile ($F_{3, 24}$ = 3.245; p = 0.040; LPS: $F_{1, 24}$ = 1.627; p = 0.214; azithromycin: $F_{1, 24}$ = 1.584; p = 0.220; Interaction: $F_{1, 24}$ = 6.525; p = 0.017) (Fig. 1B) or swimming ($K_{4, 28}$ = 10.61; p = 0.014; LPS: $F_{1, 24}$ = 6.145; p = 0.021; azithromycin: $F_{1, 24}$ = 1.924; p = 0.178; Interaction: $F_{1, 24}$ = 5.996; p = 0.022) (Supplementary Fig. S1B) during the whole test varied across the experimental conditions. No major changes were observed in the time spent climbing ($F_{3, 23}$ = 2.06; p = 0.133; LPS: $F_{1, 23}$ = 2.652; p = 0.117; azithromycin: $F_{1, 23}$ = 0.556; p = 0.464; Interaction: $F_{1, 23}$ = 2.747; p = 0.111) (Supplementary Fig. S1C). Post-hoc comparisons revealed that LPS-treated mice showed increased immobility (p = 0.012) and decreased swimming (p = 0.002) time, whereas azithromycin reversed these effects (immobility: p = 0.013; swimming: p = 0.018). Similar results were obtained in the last 5 (Supplementary Fig. S1D–I and Extended data 1) and 4 (Supplementary Fig. S1D–I and Extended data 1) min of the test.

We next examined the cellular effects induced by LPS and azithromycin administration on the DG. LPS increased the number of Fractin$^+$ apoptotic cells, an effect that was reversed by azithromycin ($F_{3, 15}$ = 25.52; p < 0.0001; LPS: $F_{1, 15}$ = 24.38; p = 0.0002; azithromycin: $F_{1, 15}$ = 38.17; p < 0.0001; Interaction: $F_{1, 15}$ = 22.79; p < 0.0002 (Fig. 1C). Accordingly, azithromycin reversed the reduced GCL volume in LPS-treated mice (post-hoc comparison *LW vs LA*: p = 0.0166) ($F_{3, 16}$ = 10.66; p = 0.014; LPS: $F_{1, 16}$ = 3.112; p = 0.0968; azithromycin: $F_{1, 16}$ = 5.666; p = 0.0301; Interaction: $F_{1, 16}$ = 1.073; p = 0.3157) (Supplementary Fig. 2A). Both LPS and azithromycin increased the expression of lectin in the GCL ($F_{3, 16}$ = 8.518; p = 0.02; LPS: $F_{1, 12}$ = 9.664; p = 0.009; azithromycin: $F_{1, 12}$ = 6.111; p = 0.0294; Interaction: $F_{1, 12}$ = 0.4054; p = 0.5363) and the ML ($F_{3, 16}$ = 10.63; p = 0.002; LPS: $F_{1, 12}$ = 21.8; p = 0.0005; azithromycin: $F_{1, 12}$ = 21.8; p = 0.0005; Interaction: $F_{1, 12}$ = 3.065; p = 0.1055) (Supplementary Fig. 2B–C), thereby reflecting the increased reactivity of this region of the brain. Accordingly, azithromycin did not reverse the increased number of Iba1$^+$ microglia caused by LPS administration ($F_{3, 16}$ = 9.66; p = 0.007; LPS: $F_{1, 13}$ = 13.95; p = 0.0025; azithromycin: $F_{1, 13}$ = 0.0002; p = 0.9962; Interaction: $F_{1, 13}$ = 0.6306; p = 0.4414) (Fig. 1D–H). The expression of pro-inflammatory cytokines, such as Eotaxin 2, Gamma interferon (IFN-γ), and tumor necrosis factor α (TNF-α), among others, was increased in response to LPS, but conversely was normalized or reduced by azithromycin (Fig. 1I and Supplementary Fig. 2E–F). The expression of other neuroprotective cytokines (such as vascular endothelial growth factor (VEGF)) was reduced after LPS administration and markedly upregulated by azithromycin (Fig. 1J and Supplementary Fig. 2E–F).

We next examined the effects of LPS and azithromycin administration on the gut microbiome (Supplementary Figs. 3 and 4). Azithromycin reduced the β- (Bray-Curtis index, *PA vs. PW:* pseudo-F = 7.132; p = 0.001) (Supplementary Fig. 3A and Extended data 1) and α-

(Shannon index, *PA* vs. *PW*: H = 9.8; p = 0.002) (Supplementary Fig. 3B and Extended data 1) diversity. Although the administration of LPS caused no major effects on these parameters (Bray-Curtis index, *LW* vs. *PW*: pseudo-F = 1.274; p = 0.093; Shannon index, *PA* vs. *PW*: H = 0.037; p = 0.949) (Supplementary Fig. 3A–B and Extended data 1), LPS-challenged mice showed a reduced presence of *Lachnospiraceae UCG-010* (q < 0.001) and *Coriobacteriaceae* UCG-002 (q < 0.001) genera. These decreases were counteracted by treatment with azithromycin (*Lachnospiraceae UCG-010* q = 0,0066; *Coriobacteriaecae UCG-002* q < 0.001). The increased presence of *Turicibacter* (q < 0.001) caused by LPS administration was not reversed by azithromycin (Supplementary Figs. S3C and S4). The aforementioned alterations in the gut microbiome composition were paralleled by functional changes in several pathways related mainly to energy utilization (Supplementary Figs. S5–S10, and Extended data 2).

3.2. Capacity of azithromycin to counteract the effects of LPS administration on AHN

We next examined the effects of LPS and azithromycin treatment on distinct cell subpopulations encompassed by AHN (Fig. 2). The population of Sox2$^+$ hippocampal neural stem cells (NSCs) was reduced upon LPS administration, whereas the opposite effect was found in response to azithromycin (F$_{3, 16}$ = 14.22; p < 0.0001; LPS: F$_{1, 16}$ = 27.25; p < 0.0001; azithromycin: F$_{1, 16}$ = 15.14; p = 0.0013; Interaction: F$_{1, 16}$ = 0.278; p = 0.6052) (Fig. 2B and F–I). No changes in the number of PH3$^+$ proliferative cells were detected (Extended data 1 and Supplementary Fig. 2D). With respect to the survival and differentiation of immature DGCs, azithromycin increased the number of DCX$^+$ (Fig. 2C and J–M) and IdU$^+$ (Fig. 2D and J–M) cells, as well as the percentage of the latter cells expressing NeuN (DCX$^+$ cells: F$_{3, 20}$ = 15.14; p = 0.002; LPS: F$_{1, 16}$ = 1.838; p = 0.194; azithromycin: F$_{1, 16}$ = 30.5; p < 0.0001; Interaction: F$_{1, 16}$ = 3.892; p = 0.0661; IdU$^+$ cells: F$_{3, 15}$ = 4.324; p = 0.0219; LPS: F$_{1, 15}$ = 0.8602; p = 0.3684; azithromycin: F$_{1, 15}$ = 10.99; p = 0.0047; Interaction: F$_{1, 15}$ = 0.5045; p = 0.4884; percentage of IdU$^+$ cells that express NeuN: F$_{3, 16}$ = 7.14; p = 0.0029; LPS: F$_{1, 16}$ = 0.013; p = 0.9107; azithromycin: F$_{1, 16}$ = 9.785; p = 0.0065;; Interaction: F$_{1, 16}$ = 11.62; p = 0.0036), thereby counteracting the negative consequences of LPS administration (post-hoc comparisons *LW* vs. *LA*: DCX$^+$ cells: p = 0.0017; IdU$^+$ cells: p = 0.0502; percentage of IdU$^+$ cells that express NeuN: p = 0.0017) (Fig. 2E,J–M and Extended data 1). Putative correlations between the numbers of distinct cell populations were evaluated (Supplementary Figs. S11 and S12 and Extended data 1). As shown, negative correlations between the number of Fractin$^+$ apoptotic cells and that of Sox2$^+$ cells (p = 0.0003) (Supplementary Fig. S11B), DCX$^+$ cells (p < 0.0001) (Supplementary Fig. S11C), IdU$^+$ cells (p = 0.0066) (Supplementary Fig. S11D), and the percentage of IdU$^+$ NeuN$^+$ cells out of total IdU$^+$ cells (p = 0.0261) (Supplementary Fig. S11E) were observed. Conversely, positive correlations between the number of Sox2$^+$ and DCX$^+$ cells (p = 0.0032) (Supplementary Fig. S11N), Sox2$^+$ and IdU$^+$ cells (p = 0.0038) (Supplementary Fig. S11B), DCX$^+$ and IdU$^+$ cells (p = 0.0032) (Supplementary Fig. S12A), the number of DCX$^+$ cells and the percentage of IdU$^+$ NeuN$^+$ cells out of total IdU$^+$ cells (p = 0.0003) (Supplementary Fig. S12C), and the number of DCX$^+$ and PH3$^+$ cells (p = 0.0171) (Supplementary Fig. S12D), among others, were detected (Extended data 1).

Subsequently, the morphological maturation of newborn DGCs was studied at two time points, namely 2 (early, Fig. 3) and 8 (late, Fig. 4) weeks post-infection. Early neuronal maturation was affected by treatment with LPS and azithromycin (Fig. 3A–J). In this regard, the total dendritic length (Fig. 3F), length of the primary apical dendrite (Fig. 3G), migration towards the GCL (Fig. 3H), percentage of cells with several primary apical dendrites (Fig. 3I), and dendritic branching in Sholĺs analysis (Fig. 3J) were negatively affected by LPS administration. Azithromycin reversed most of these alterations (total dendritic length: F$_{3, 218}$ = 19.93; p < 0.0001; LPS: F$_{1, 215}$ = 15.92; p < 0.0001;

azithromycin: F$_{1, 215}$ = 4.905; p = 0.0278; Interaction: F$_{1, 215}$ = 38.09; p < 0.0001; length of the primary apical dendrite: F$_{3, 250}$ = 40.12; p < 0.0001; LPS: F$_{1, 246}$ = 24.36; p < 0.0001; azithromycin: F$_{1, 246}$ = 28.7; p < 0.0001; Interaction: F$_{1, 246}$ = 0.0138; p = 0.9068; migration towards the GCL: F$_{3, 307}$ = 80.27; p < 0.0001; LPS: F$_{1, 303}$ = 20.7; p < 0.0001; azithromycin: F$_{1, 303}$ = 28.73; p < 0.0001; Interaction: F$_{1, 303}$ = 19.05; p < 0.0001; and percentage of cells with several primary apical dendrites: $\chi^2_{3, 320}$ = 39.364; p < 0.0001: *LW* vs. *LA*: p < 0.0001; Sholĺs analysis Épsilon Greenhouse-Geisser: Distance * Experimental group: p < 0.0001) (Extended data 1).

Similarly, chronic LPS administration for 8 weeks impaired the late morphological maturation of newborn DGCs (Llorens-Martin et al., 2014) (Fig. 4A–J). Specifically, it decreased the total dendritic length (Fig. 4F), length of the primary apical dendrite (Fig. 4G), and dendritic branching in Sholĺs analysis (Fig. 4J), as well as increasing migration towards the GCL (Fig. 4H) and the percentage of cells with several primary apical dendrites (Fig. 4I). Azithromycin fully reversed these morphological alterations (total dendritic length: F$_{3, 164}$ = 44.93; p < 0.0001; LPS: F$_{1, 160}$ = 6.19; p = 0.0139; azithromycin: F$_{1, 160}$ = 23.16; p < 0.0001; Interaction: F$_{1, 160}$ = 16.72; p = 0.0001; length of the primary apical dendrite: F$_{3, 278}$ = 27.11; p < 0.0001; LPS: F$_{1, 274}$ = 10.72; p = 0.0012; azithromycin: F$_{1, 274}$ = 0.2063; p = 0.65; Interaction: F$_{1, 274}$ = 21.15; p < 0.0001; migration towards the GCL: F$_{3, 291}$ = 38.93; p < 0.0001; LPS: F$_{1, 287}$ = 9.905; p = 0.0018; azithromycin: F$_{1, 287}$ = 11.57; p = 0.0008; Interaction: F$_{1, 287}$ 34.11; p < 0.0001; and percentage of cells with several primary apical dendrites: $\chi^2_{3, 293}$ = 8.101; p = 0.044: *LW* vs. *LA*: p = 0.015; Sholĺs analysis Épsilon Greenhouse-Geisser: Distance * Experimental group: p < 0.0001) (Extended data 1).

To assess the effects of these treatments on the functional output of newborn DGCs, we used a Syn:GFP-encoding retrovirus (Kelsch et al., 2009). LPS administration impaired the establishment of efferent synaptic contacts at the MFTs of newborn DGCs (Fig. 4K–Q). It increased the area of the former structures (Fig. 4O) but reduced the number of filopodia (Fig. 4P) and the active area occupied by Syn$^+$ clusters (Fig. 4Q). Importantly, azithromycin fully reversed these effects (MFT area: F$_{3, 1330}$ = 74.74; p < 0.0001; LPS: F$_{1, 1326}$ = 40.16; p < 0.0001; azithromycin: F$_{1, 1326}$ = 5.01; p = 0.0254; Interaction: F$_{1, 1326}$ = 24.28; p < 0.0001; number of filopodia: F$_{3, 1222}$ = 132.7; p < 0.0001; LPS: F$_{1, 1218}$ = 18.17; p < 0.0001; azithromycin: F$_{1, 1218}$ = 46.41; p < 0.0001; Interaction: F$_{1, 1218}$ = 69.91; p < 0.0001; and MFT Syn$^+$ active area F$_{3, 1330}$ = 349.5; p < 0.0001; LPS: F$_{1, 1326}$ = 35.46; p < 0.0001; azithromycin: F$_{1, 1326}$ = 196.2; p < 0.0001; Interaction: F$_{1, 1326}$ = 208.8; p < 0.0001).

The administration of LPS for 8 weeks increased the number of Iba1$^+$ cells (Fig. 4R–V) and the expression of CD68 in these cells (Fig. 4W–AA), thereby indicating persistent microglia activation. These effects were reversed by azithromycin (Number of Iba1$^+$ cells: F$_{3, 27}$ = 13.32; p < 0.0001; LPS: F$_{1, 27}$ = 9.32; p = 0.005; azithromycin: F$_{1, 27}$ = 24.1; p < 0.0001; Interaction: F$_{1, 27}$ = 5.181; p = 0.031; CD68 expression: F$_{3, 73}$ = 32.34; p < 0.0001; LPS: F$_{1, 69}$ = 24.69; p < 0.0001; azithromycin: F$_{1, 69}$ = 0.3198; p = 0.5736; Interaction: F$_{1, 69}$ = 11.92; p = 0.001) (Fig. 4R–AA). Accordingly, LPS reduced the length of microglial processes, whereas azithromycin had the opposite effect (F$_{3, 96}$ = 16.86; p = 0.0008; LPS: F$_{1, 92}$ = 6.802; p = 0.0106; azithromycin: F$_{1, 92}$ = 5.303; p = 0.0235; Interaction: F$_{1, 92}$ = 8.237; p = 0.0051) (Fig. 4AB and Extended data 1).

Taken together, these data indicate that azithromycin exerts robust neuroprotective effects in the murine hippocampus that are paralleled by the reversion of pro-inflammatory changes and AHN impairments induced by LPS.

4. Discussion

The hippocampus acts as a central hub in the processing of sensory information. The continuous incorporation of new neurons through AHN partly underlies the enhanced neural plasticity held by this

structure. AHN plays a key role in the regulation of episodic memory, forgetting, and mood (Akers et al., 2014; Hill et al., 2015; Sahay et al., 2011). The generation of new neurons in the adult hippocampus has been reported in more than 120 mammalian species (reviewed in (Terreros-Roncal et al., 2022)), including humans (Eriksson et al., 1998; Moreno-Jimenez et al., 2019). Resident hippocampal NSCs with astrocyte-like properties (Seri et al., 2001) sustain the capacity of the DG to produce new DGCs throughout life. During AHN, neural precursors first divide actively. Subsequently, they exit the cell cycle and become committed to the neuronal lineage. After going through sequential maturation stages, newborn DGCs progressively increase the complexity of their dendritic trees (Zhao et al., 2006), which results in their functional integration into the trisynaptic circuits of the hippocampus (Kempermann et al., 2004). In this regard, the use of genetically engineered retroviruses has been instrumental in assessing the establishment of afferent and efferent synaptic contacts (Kelsch et al., 2008; Kelsch et al., 2009; Llorens-Martin et al., 2013; Llorens-Martin et al., 2015a), thereby allowing the study of the functional maturation of these cells.

Each of the stages encompassed by AHN can be either positively or negatively modulated by extrinsic factors. In this regard, several pathological conditions (Gould et al., 1997; Monje et al., 2003) are paralleled by a remarkable surge in hippocampal neuroinflammation, which impairs newborn DGC maturation (Llorens-Martin et al., 2016; Llorens-Martin et al., 2014; Terreros-Roncal et al., 2021). In fact, these cells show an aberrant morphological phenotype in experimental models of acute stress (Llorens-Martin et al., 2016), sepsis (Llorens-Martin et al., 2014), and neurodegenerative diseases (Llorens-Martin et al., 2013; Terreros-Roncal et al., 2019), as well as in patients with the latter conditions (Marquez-Valadez et al., 2022; Terreros-Roncal et al., 2019). In particular, the altered phenotype exhibited by these cells is characterized by the presence of several primary apical dendrites, distal dendritic atrophy, and a reduced number of synaptic contacts (both at the excitatory afferent and efferent levels). Moreover, here we show, for the first time, that LPS challenge reduces the number of filopodia in newborn DGC MFTs. This observation points to the impaired synaptic output of these cells onto CA3 inhibitory interneurons (Restivo et al., 2015). These alterations, together with the reduction in the excitatory connections caused by LPS administration previously described (Llorens-Martin et al., 2014), are expected to cause an overall disconnection of newborn DGCs from the entire hippocampal circuitry, thereby contributing to the alteration of hippocampal-dependent behaviors (Llorens-Martin et al., 2015b). Indeed, LPS challenge triggers a depression-like phenotype (Dunn and Swiergiel, 2005) and impedes pattern-separation (Llorens-Martin et al., 2014)—two types of behavior suggested to be related to AHN (Hill et al., 2015; Malberg et al., 2000; Sahay et al., 2011). In fact, time spent immobile during the Porsolt test inversely correlates with the rate of AHN and the number of DCX$^+$ immature DGCs in mice (Llorens-Martin et al., 2007).

Here we addressed the capacity of azithromycin to counteract the negative consequences of peripheral LPS administration in mice. Azithromycin is a broad-spectrum macrolide antibiotic commonly used to treat infections caused by distinct bacteria. Moreover, it is used as an immunomodulatory drug to treat patients with chronic inflammatory diseases. Azithromycin not only has higher tissue penetration than other antibiotics but it also presents a biphasic elimination profile that renders slow tissue clearance (Davila et al., 1991), thereby showing efficacy in chronic treatments (Dumas et al., 1994) and contributing to LPS tolerance (Bosnar et al., 2013). Our data suggest that azithromycin exerts neuroprotective effects at the hippocampal level and that these effects are likely to be mediated by at least 3 distinct mechanisms.

First, some of the anti-inflammatory actions of azithromycin have been suggested to be indirect and derived from its anti-microbial properties (Hao et al., 2013; Kamemoto et al., 2009). In this regard, our data show that azithromycin counteracts the LPS-driven reduction of *Lachnospiraceae* UCG-010 and Coriobacteriaceae UCG-002 genera in the fecal microbiome (Supplementary Figs. S3 and S4). These data gain

further relevance in light of the functional changes in the gut microbiota caused by LPS administration (Supplementary Fig. S5 and Extended data 2), some of which are reversed by azithromycin (Supplementary Fig. S8 and Extended data 2). These pathways are related to the utilization of energy sources and the production of distinct metabolites, such as short-chain fatty acids, which are relevant for brain function. Strikingly, *Lachnospiraceae* UCG-010 are considered to be one of the main sources of short-chain fatty acids in the intestine (Vacca et al., 2020). These molecules control microglia activation, maturation, and differentiation and exert neuroprotective actions through the modulation of various microglial functions (Cryan et al., 2019; Erny et al., 2015). Interestingly, enhanced proliferation of *Lachnospiraceae* UCG-010 has been associated with the amelioration of cognitive impairments and a reduction in neuroinflammation in a mouse model of Alzheimer's disease (Zhang et al., 2023). Therefore, given the increase in the abundance of this genus caused by azithromycin, our data suggest that some of the neuroprotective actions exerted by this antibiotic are related to the functional remodeling of the gut microbiome.

Second, azithromycin inhibits the production of pro-inflammatory cytokines and activates regulatory functions in macrophages in a cell-autonomous manner (Choi et al., 2014; Tong et al., 2011; Venditto et al., 2021). Under several pathological conditions, the release of pro-inflammatory cytokines, such as TNF-α, IL-1β, monocyte chemo-attractant protein (MCP)-1, and macrophage inflammatory protein (MIP)-1α, underlie macrophage/microglia-induced brain damage. In response to LPS, azithromycin reduces blood–brain barrier damage, and the cerebral infiltration of neutrophils, and inflammatory macrophages in a dose-dependent manner (Amantea et al., 2016). Here we show that it also normalizes the level of pro-inflammatory cytokines in the DG (Fig. 1), thereby putatively remodeling the hippocampal inflammatory milieu. This remodeling is paralleled by morphological and functional changes in DG microglia after chronic treatment. These effects are in agreement with the capacity of this antibiotic to polarize microglia/macrophages towards neuroprotective phenotypes (Amantea et al., 2016; Easton, 2013; Murphy et al., 2008; Petrelli et al., 2016; Zhang et al., 2019) through the inhibition of the NF-kB and STAT1 pathways (Amantea et al., 2019; Haydar et al., 2019; Venditto et al., 2021). Microglia play a prominent role in the regulation of AHN (Sierra et al., 2010). They eliminate dysfunctional cells through an apoptosis-coupled phagocytosis mechanism (Sierra et al., 2010) and participate in synaptic pruning (Araki et al., 2020). Therefore, it can be hypothesized that azithromycin, at least in part, restores AHN through non-cell-autonomous mechanisms related to the attenuation of neuroinflammation and the modulation of microglial functions.

Third, in addition to the aforementioned non-cell autonomous actions, azithromycin phosphorylates S6 ribosomal protein, a downstream effector of mammalian target of rapamycin (mTOR) (Huang et al., 2021). Strikingly, one of the two multi-protein complexes formed by mTOR, namely Mechanistic target of rapamycin complex 1 (mTORC1), is a cornerstone in the regulation of developmental and adult neurogenesis. In this regard, the cell-autonomous activation of mTORC1 induces the terminal differentiation of NSCs and increases the production of new neurons in the neonatal subventricular zone (Mahoney et al., 2016). Similarly, the activation of mTORC1 increases the number of DCX$^+$ neuroblasts and Mash1$^+$ NSCs but does not induce NSC proliferation in adult neurogenic niches (Mahoney et al., 2016). Our data reveal that some of the stages encompassed by AHN appear to be independently regulated by the distinct experimental conditions, whereas parallel fluctuations in the number of other neurogenic cell populations are observed (Supplementary Figs. S11 and 12 and Extended data 1). For instance, azithromycin does not trigger changes in cell proliferation. Conversely, this antibiotic prevents a decrease in both the number of NSCs and immature neurons in LPS-challenged mice. Moreover, it normalizes the functional maturation of the latter, promoting the establishment of functional efferent synapses onto both excitatory and inhibitory target cells. Interestingly, these effects on AHN are paralleled

by the amelioration of cognitive deficits (Amantea et al., 2016) and the reduction in the time spent immobile during the Porsolt test in LPS-treated mice. Further studies are needed to assess the duration of the pro-neurogenic effects of azithromycin and whether these actions are relevant in severe cases of, for instance, permanent post-sepsis cognitive impairments.

Taken together, these results support the notion that azithromycin exerts potent neuroprotective effects on AHN, the hippocampal inflammatory milieu, and hippocampal-dependent behavior under pro-inflammatory conditions. These effects are likely to be orchestrated by additive cell-autonomous and non-cell-autonomous mechanisms, both at the local and peripheral levels. These data might be clinically relevant and successfully exploited under certain pathological conditions that threaten hippocampal integrity under increased levels of central or peripheral inflammation.

Author contributions

Conceptualization: FC and MLLM. Investigation: CBRM, HCR, MFG, JTR, EPMJ, NPB, FC, and MLLM. Formal analysis and data curation: CBRM, HCR, JTR, NPB, CB, ML, FC, and MLLM. . Funding acquisition: MLLM. Writing - original draft: MLLM. Writing - review & editing: CBRM, HCR, JTR, MFG, EPMJ, NPB, CB, ML, FC, and MLLM.

Declaration of competing interest

The authors declare that they have no known competing financial interests or personal relationships that could have appeared to influence the work reported in this paper.

Data availability

Data will be made available on request.

Acknowledgements

Appendix A. Supplementary data

Supplementary data to this article can be found online at https://doi.org/10.1016/j.bbi.2024.01.005.

References

Akers, K.G., Martinez-Canabal, A., Restivo, L., Yiu, A.P., De Cristofaro, A., Hsiang, H.L., Wheeler, A.L., Guskjolen, A., Niibori, Y., Shoji, H., Ohira, K., Richards, B.A., Miyakawa, T., Josselyn, S.A., Frankland, P.W., 2014. Hippocampal neurogenesis regulates forgetting during adulthood and infancy. Science 344, 598–602.

Altman, J., 1963. Autoradiographic investigation of cell proliferation in the brains of rats and cats. Anat. Rec. 145, 573–591.

Amantea, D., Bagetta, G., 2016. Drug repurposing for immune modulation in acute ischemic stroke. Curr. Opin. Pharmacol. 26, 124–130.

Amantea, D., Certo, M., Petrelli, F., Tassorelli, C., Micieli, G., Corasaniti, M.T., Puccetti, P., Fallarino, F., Bagetta, G., 2016. Azithromycin protects mice against ischemic stroke injury by promoting macrophage transition towards M2 phenotype. Exp. Neurol. 275 (Pt 1), 116–125.

Amantea, D., Petrelli, F., Greco, R., Tassorelli, C., Corasaniti, M.T., Tonin, P., Bagetta, G., 2019. Azithromycin affords neuroprotection in rat undergone transient focal cerebral ischemia. Front. Neurosci. 13, 1256.

Araki, T., Ikegaya, Y., Koyama, R., 2020. The effects of microglia- and astrocyte-derived factors on neurogenesis in health and disease. The European Journal of Neuroscience.

Benjamini, Y., Hochberg, Y., 1995. Controlling the False Discovery Rate: A Practical and Powerful Approach to Multiple Testing. J. Roy. Stat. Soc.: Ser. B (Methodol.) 57, 11.

Bolyen, E., Rideout, J.R., Dillon, M.R., Bokulich, N.A., Abnet, C.C., Al-Ghalith, G.A., Alexander, H., Alm, E.J., Arumugam, M., Asnicar, F., Bai, Y., Bisanz, J.E., Bittinger, K., Brejnrod, A., Brislawn, C.J., Brown, C.T., Callahan, B.J., Caraballo-Rodriguez, A.M., Chase, J., Cope, E.K., Da Silva, R., Diener, C., Dorrestein, P.C., Douglas, G.M., Durall, D.M., Duvallet, C., Edwardson, C.F., Ernst, M., Estaki, M., Fouquier, J., Gauglitz, J.M., Gibbons, S.M., Gibson, D.L., Gonzalez, A., Gorlick, K., Guo, J., Hillmann, B., Holmes, S., Holste, H., Huttenhower, C., Huttley, G.A., Janssen, S., Jarmusch, A.K., Jiang, L., Kaehler, B.D., Kang, K.B., Keefe, C.R., Keim, P., Kelley, S.T., Knights, D., Koester, I., Kosciolek, T., Kreps, J., Langille, M.G.I., Lee, J., Ley, R., Liu, Y.X., Loftfield, E., Lozupone, C., Maher, M., Marotz, C., Martin, B.D., McDonald, D., McIver, L.J., Melnik, A.V., Metcalf, J.L., Morgan, S.C., Morton, J.T., Naimey, A.T., Navas-Molina, J.A., Nothias, L.F., Orchanian, S.B., Pearson, T., Peoples, S.L., Petras, D., Preuss, M.L., Pruesse, E., Rasmussen, L.B., Rivers, A., Robeson 2nd, M.S., Rosenthal, P., Segata, N., Shaffer, M., Shiffer, A., Sinha, R., Song, S.J., Spear, J.R., Swafford, A.D., Thompson, L.R., Torres, P.J., Trinh, P., Tripathi, A., Turnbaugh, P.J., Ul-Hasan, S., van der Hooft, J.J.J., Vargas, F., Vazquez-Baeza, Y., Vogtmann, E., von Hippel, M., Walters, W., Wan, Y., Wang, M., Warren, J., Weber, K.C., Williamson, C.H.D., Willis, A.D., Xu, Z.Z., Zaneveld, J.R., Zhang, Y., Zhu, Q., Knight, R., Caporaso, J.G., 2019. Reproducible, interactive, scalable and extensible microbiome data science using QIIME 2. Nat. Biotechnol. 37, 852–857.

Bosnar, M., Dominis-Kramaric, M., Nujic, K., Stupin Polancec, D., Marjanovic, N., Glojnaric, I., Erakovic Haber, V., 2013. Immunomodulatory effects of azithromycin on the establishment of lipopolysaccharide tolerance in mice. Int. Immunopharmacol. 15, 498–504.

Browne, C.A., Clarke, G., Fitzgerald, P., O'Sullivan, J., Dinan, T.G., Cryan, J.F., 2022. Distinct post-sepsis induced neurochemical alterations in two mouse strains. Brain Behav. Immun. 104, 39–53.

Callahan, B.J., McMurdie, P.J., Rosen, M.J., Han, A.W., Johnson, A.J., Holmes, S.P., 2016. DADA2: High-resolution sample inference from Illumina amplicon data. Nat. Methods 13, 581–583.

Choi, E.Y., Jin, J.Y., Choi, J.I., Choi, I.S., Kim, S.J., 2014. Effect of azithromycin on Prevotella intermedia lipopolysaccharide-induced production of interleukin-6 in murine macrophages. Eur. J. Pharmacol. 729, 10–16.

Cryan, J.F., O'Riordan, K.J., Cowan, C.S.M., Sandhu, K.V., Bastiaanssen, T.F.S., Boehme, M., Codagnone, M.G., Cussotto, S., Fulling, C., Golubeva, A.V., Guzzetta, K. E., Jaggar, M., Long-Smith, C.M., Lyte, J.M., Martin, J.A., Molinero-Perez, A., Moloney, G., Morelli, E., Morillas, E., O'Connor, R., Cruz-Pereira, J.S., Peterson, V.L., Rea, K., Ritz, N.L., Sherwin, E., Spichak, S., Teichman, E.M., van de Wouw, M., Ventura-Silva, A.P., Wallace-Fitzsimons, S.E., Hyland, N., Clarke, G., Dinan, T.G., 2019. The Microbiota-gut-brain axis. Physiol. Rev. 99, 1877–2013.

Davila, D., Kolacny-Babic, L., Plavsic, F., 1991. Pharmacokinetics of azithromycin after single oral dosing of experimental animals. Biopharm. Drug Dispos. 12, 505–514.

Detke, M.J., Rickels, M., Lucki, I., 1995. Active behaviors in the rat forced swimming test differentially produced by serotonergic and noradrenergic antidepressants. Psychopharmacology 121, 66–72.

Douglas, G.M., Maffei, V.J., Zaneveld, J.R., Yurgel, S.N., Brown, J.R., Taylor, C.M., Huttenhower, C., Langille, M.G.I., 2020. PICRUSt2 for prediction of metagenome functions. Nat. Biotechnol. 38, 685–688.

Dumas, J.L., Chang, R., Mermillod, B., Piguet, P.F., Comte, R., Pechere, J.C., 1994. Evaluation of the efficacy of prolonged administration of azithromycin in a murine model of chronic toxoplasmosis. J. Antimicrob. Chemother. 34, 111–118.

Dunn, A.J., Swiergiel, A.H., 2005. Effects of interleukin-1 and endotoxin in the forced swim and tail suspension tests in mice. Pharmacol. Biochem. Behav 81, 688–693.

Easton, A.S., 2013. Neutrophils and stroke - can neutrophils mitigate disease in the central nervous system? Int. Immunopharmacol. 17, 1218–1225.

Equi, A., Balfour-Lynn, I.M., Bush, A., Rosenthal, M., 2002. Long term azithromycin in children with cystic fibrosis: a randomised, placebo-controlled crossover trial. Lancet 360, 978–984.

Eriksson, P.S., Perfilieva, E., Bjork-Eriksson, T., Alborn, A.M., Nordborg, C., Peterson, D. A., Gage, F.H., 1998. Neurogenesis in the adult human hippocampus. Nat. Med. 4, 1313–1317.

Erny, D., Hrabe de Angelis, A.L., Jaitin, D., Wieghofer, P., Staszewski, O., David, E., Keren-Shaul, H., Mahlakoiv, T., Jakobshagen, K., Buch, T., Schwierzeck, V., Utermohlen, O., Chun, E., Garrett, W.S., McCoy, K.D., Diefenbach, A., Staeheli, P., Stecher, B., Amit, I., Prinz, M., 2015. Host microbiota constantly control maturation and function of microglia in the CNS. Nat. Neurosci. 18, 965–977.

Gould, E., McEwen, B.S., Tanapat, P., Galea, L.A., Fuchs, E., 1997. Neurogenesis in the dentate gyrus of the adult tree shrew is regulated by psychosocial stress and NMDA receptor activation. J. Neurosci. 17, 2492–2498.

Grabrucker, S., Marizzoni, M., Silajdzic, E., Lopizzo, N., Mombelli, E., Nicolas, S., Dohm-Hansen, S., Scassellati, C., Moretti, D.V., Rosa, M., Hoffmann, K., Cryan, J.F., O'Leary, O.F., English, J.A., Lavelle, A., O'Neill, C., Thuret, S., Cattaneo, A., Nolan,

Y.M., 2023. Microbiota from Alzheimer's patients induce deficits in cognition and hippocampal neurogenesis. Brain : a journal of neurology.

Guzzetta, K.E., Cryan, J.F., O'Leary, O.F., 2022. Microbiota-Gut-Brain Axis Regulation of Adult Hippocampal Neurogenesis. Brain Plast. 8, 97–119.

Hao, K., Qi, Q., Hao, H., Wang, G., Chen, Y., Liang, Y., Xie, L., 2013. The pharmacokinetic-pharmacodynamic model of azithromycin for lipopolysaccharide-induced depressive-like behavior in mice. PLoS One 8, e54981.

Haydar, D., Cory, T.J., Birket, S.E., Murphy, B.S., Pennypacker, K.R., Sinai, A.P., Feola, D. J., 2019. Azithromycin Polarizes Macrophages to an M2 Phenotype via Inhibition of the STAT1 and NF-kappaB Signaling Pathways. J. Immunol. 203, 1021–1030.

Hill, A.S., Sahay, A., Hen, R., 2015. Increasing adult hippocampal neurogenesis is sufficient to reduce anxiety and depression-like behaviors. Neuropsychopharmacology 40, 2368–2378.

Holm, S., 1979. A simple sequentially rejective multiple test procedure. Scand. J. Stat. 6, 6.

Huang, J., Li, Z., Hu, Y., Chen, G., Li, Z., Xie, Y., Huang, H., Su, W., Chen, X., Liang, D., 2021. Azithromycin modulates Teff/Treg balance in retinal inflammation via the mTOR signaling pathway. Biochem. Pharmacol. 193, 114793.

Kaehler, B.D., Bokulich, N.A., McDonald, D., Knight, R., Caporaso, J.G., Huttley, G.A., 2019. Species abundance information improves sequence taxonomy classification accuracy. Nat. Commun. 10, 4643.

Kamemoto, A., Ara, T., Hattori, T., Fujinami, Y., Imamura, Y., Wang, P.L., 2009. Macrolide antibiotics like azithromycin increase lipopolysaccharide-induced IL-8 production by human gingival fibroblasts. Eur. J. Med. Res. 14, 309–314.

Kang, J.Y., Jo, M.R., Kang, H.H., Kim, S.K., Kim, M.S., Kim, Y.H., Kim, S.C., Kwon, S.S., Lee, S.Y., Kim, J.W., 2016. Long-term azithromycin ameliorates not only airway inflammation but also remodeling in a murine model of chronic asthma. Pulm. Pharmacol. Ther. 36, 37–45.

Kelsch, W., Lin, C.W., Lois, C., 2008. Sequential development of synapses in dendritic domains during adult neurogenesis. Proceedings of the National Academy of Sciences of the United States of America 105, 16803-16808.

Kelsch, W., Lin, C.W., Mosley, C.P., Lois, C., 2009. A critical period for activity-dependent synaptic development during olfactory bulb adult neurogenesis. J. Neurosci. 29, 11852–11858.

Kelsch, W., Sim, S., Lois, C., 2010. Watching synaptogenesis in the adult brain. Annu. Rev. Neurosci. 33, 131–149.

Kempermann, G., Jessberger, S., Steiner, B., Kronenberg, G., 2004. Milestones of neuronal development in the adult hippocampus. Trends in Neuroscience 27, 447–452.

Kitsiouli, E., Antoniou, G., Gotzou, H., Karagiannopoulos, M., Basagiannis, D., Christoforidis, S., Nakos, G., Lekka, M.E., 2015. Effect of azithromycin on the LPS-induced production and secretion of phospholipase A2 in lung cells. BBA 1852, 1288–1297.

Klindworth, A., Pruesse, E., Schweer, T., Peplies, J., Quast, C., Horn, M., Glockner, F.O., 2013. Evaluation of general 16S ribosomal RNA gene PCR primers for classical and next-generation sequencing-based diversity studies. Nucleic Acids Res. 41, e1.

Kozorovitskiy, Y., Gould, E., 2004. Dominance hierarchy influences adult neurogenesis in the dentate gyrus. J. Neurosci. 24, 6755–6759.

Lin, H., Peddada, S.D., 2020. Analysis of compositions of microbiomes with bias correction. Nat. Commun. 11, 3514.

Llorens-Martin, M., Fuster-Matanzo, A., Teixeira, C.M., Jurado-Arjona, J., Ulloa, F., Defelipe, J., Rabano, A., Hernandez, F., Soriano, E., Avila, J., 2013. GSK-3beta overexpression causes reversible alterations on postsynaptic densities and dendritic morphology of hippocampal granule neurons in vivo. Mol. Psychiatry 18, 451–460.

Llorens-Martin, M., Jurado-Arjona, J., Fuster-Matanzo, A., Hernandez, F., Rabano, A., Avila, J., 2014. Peripherally triggered and GSK-3beta-driven brain inflammation differentially skew adult hippocampal neurogenesis, behavioral pattern separation and microglial activation in response to ibuprofen. Transl. Psychiatry 4, e463.

Llorens-Martin, M., Jurado-Arjona, J., Avila, J., Hernandez, F., 2015a. Novel connection between newborn granule neurons and the hippocampal CA2 field. Exp. Neurol. 263, 285–292.

Llorens-Martin, M., Rabano, A., Avila, J., 2015b. The Ever-Changing Morphology of Hippocampal Granule Neurons in Physiology and Pathology. Front. Neurosci. 9, 526.

Llorens-Martin, M., Jurado-Arjona, J., Bolos, M., Pallas-Bazarra, N., Avila, J., 2016. Forced swimming sabotages the morphological and synaptic maturation of newborn granule neurons and triggers a unique pro-inflammatory milieu in the hippocampus. Brain Behav. Immun. 53, 242–254.

Llorens-Martin, M.V., Rueda, N., Martinez-Cue, C., Torres-Aleman, I., Florez, J., Trejo, J. L., 2007. Both increases in immature dentate neuron number and decreases of immobility time in the forced swim test occurred in parallel after environmental enrichment of mice. Neuroscience 147, 631–638.

Llorens-Martin, M., Torres-Aleman, I., Trejo, J.L., 2006. Pronounced individual variation in the response to the stimulatory action of exercise on immature hippocampal neurons. Hippocampus 16, 480–490.

Llorens-Martin, M., Tejeda, G.S., Trejo, J.L., 2010. Differential regulation of the variations induced by environmental richness in adult neurogenesis as a function of time: a dual birthdating analysis. PLoS One 5, e12188.

Lucassen, P.J., Meerlo, P., Naylor, A.S., van Dam, A.M., Dayer, A.G., Fuchs, E., Oomen, C. A., Czeh, B., 2010. Regulation of adult neurogenesis by stress, sleep disruption, exercise and inflammation: Implications for depression and antidepressant action. Eur. Neuropsychopharmacol. 20, 1–17.

Lugert, S., Basak, O., Knuckles, P., Haussler, U., Fabel, K., Gotz, M., Haas, C.A., Kempermann, G., Taylor, V., Giachino, C., 2010. Quiescent and active hippocampal neural stem cells with distinct morphologies respond selectively to physiological and pathological stimuli and aging. Cell Stem Cell 6, 445–456.

Mahoney, C., Feliciano, D.M., Bordey, A., Hartman, N.W., 2016. Switching on mTORC1 induces neurogenesis but not proliferation in neural stem cells of young mice. Neurosci. Lett. 614, 112–118.

Malberg, J.E., Eisch, A.J., Nestler, E.J., Duman, R.S., 2000. Chronic antidepressant treatment increases neurogenesis in adult rat hippocampus. J. Neurosci. 20, 9104–9110.

Marquez-Valadez, B., Rabano, A., Llorens-Martin, M., 2022. Progression of Alzheimer's disease parallels unusual structural plasticity of human dentate granule cells. Acta Neuropathol. Commun. 10, 125.

Monje, M.L., Toda, H., Palmer, T.D., 2003. Inflammatory blockade restores adult hippocampal neurogenesis. Science 302, 1760–1765.

Moreno-Jimenez, E.P., Flor-Garcia, M., Terreros-Roncal, J., Rabano, A., Cafini, F., Pallas-Bazarra, N., Avila, J., Llorens-Martin, M., 2019. Adult hippocampal neurogenesis is abundant in neurologically healthy subjects and drops sharply in patients with Alzheimer's disease. Nat. Med. 25, 554–560.

Morris, R., Armbruster, K., Silva, J., Widell, D.J., Cheng, F., 2020. The Association between the Usage of Non-Steroidal Anti-Inflammatory Drugs and Cognitive Status: Analysis of Longitudinal and Cross-Sectional Studies from the Global Alzheimer's Association Interactive Network and Transcriptomic Data. Brain sciences 10.

Murphy, B.S., Sundareshan, V., Cory, T.J., Hayes Jr., D., Anstead, M.I., Feola, D.J., 2008. Azithromycin alters macrophage phenotype. J. Antimicrob. Chemother. 61, 554–560.

Ogbonnaya, E.S., Clarke, G., Shanahan, F., Dinan, T.G., Cryan, J.F., O'Leary, O.F., 2015. Adult Hippocampal Neurogenesis Is Regulated by the Microbiome. Biol. Psychiatry 78, e7–e9.

Pakkenberg, B., Gundersen, H.J., 1988. Total number of neurons and glial cells in human brain nuclei estimated by the disector and the fractionator. J. Microsc. 150, 1–20.

Pallas-Bazarra, N., Jurado-Arjona, J., Navarrete, M., Esteban, J.A., Hernandez, F., Avila, J., Llorens-Martin, M., 2016. Novel function of Tau in regulating the effects of external stimuli on adult hippocampal neurogenesis. EMBO J. 35, 1417–1436.

Pallas-Bazarra, N., Kastanauskaite, A., Avila, J., DeFelipe, J., Llorens-Martin, M., 2017. GSK-3beta Overexpression Alters the Dendritic Spines of Developmentally Generated Granule Neurons in the Mouse Hippocampal Dentate Gyrus. Front. Neuroanat. 11, 18.

Pedregosa, F.V., Gramfort, G., Michel, A., Thirion, V., Grisel, B., Blondel, O., Prettenhofer, M., Weiss, P., Dubourg, R., Vanderplas, V., Passos, J., Cournapeau, A., Brucher, D., Perrot, M., Duchesnay, E., 2011. Scikit-learn: machine learning in python. J. Mach. Learn. Res. 12, 5.

Petrelli, F., Muzzi, M., Chiarugi, A., Bagetta, G., Amantea, D., 2016. Poly(ADP-ribose) polymerase is not involved in the neuroprotection exerted by azithromycin against ischemic stroke in mice. Eur. J. Pharmacol. 791, 518–522.

Restivo, L., Niibori, Y., Mercaldo, V., Josselyn, S.A., Frankland, P.W., 2015. Development of Adult-Generated Cell Connectivity with Excitatory and Inhibitory Cell Populations in the Hippocampus. J. Neurosci. 35, 10600–10612.

Retallack, H., Di Lullo, E., Arias, C., Knopp, K.A., Laurie, M.T., Sandoval-Espinosa, C., Mancia Leon, W.R., Krencik, R., Ullian, E.M., Spatazza, J., Pollen, A.A., Mandel-Brehm, C., Nowakowski, T.J., Kriegstein, A.R., DeRisi, J.L., 2016. Zika virus cell tropism in the developing human brain and inhibition by azithromycin. Proceedings of the National Academy of Sciences of the United States of America 113, 14408-14413.

Sahay, A., Scobie, K.N., Hill, A.S., O'Carroll, C.M., Kheirbek, M.A., Burghardt, N.S., Fenton, A.A., Dranovsky, A., Hen, R., 2011. Increasing adult hippocampal neurogenesis is sufficient to improve pattern separation. Nature 472, 466–470.

Segata, N., Izard, J., Waldron, L., Gevers, D., Miropolsky, L., Garrett, W.S., Huttenhower, C., 2011. Metagenomic biomarker discovery and explanation. Genome Biol. 12, R60.

Seri, B., Garcia-Verdugo, J.M., McEwen, B.S., Alvarez-Buylla, A., 2001. Astrocytes give rise to new neurons in the adult mammalian hippocampus. J. Neurosci. 21, 7153–7160.

Sherwin, E., Rea, K., Dinan, T.G., Cryan, J.F., 2016. A gut (microbiome) feeling about the brain. Curr. Opin. Gastroenterol. 32, 96–102.

Sierra, A., Encinas, J.M., Deudero, J.J., Chancey, J.H., Enikolopov, G., Overstreet-Wadiche, L.S., Tsirka, S.E., Maletic-Savatic, M., 2010. Microglia shape adult hippocampal neurogenesis through apoptosis-coupled phagocytosis. Cell Stem Cell 7, 483–495.

Terreros-Roncal, J., Flor-Garcia, M., Moreno-Jimenez, E.P., Pallas-Bazarra, N., Rabano, A., Sah, N., van Praag, H., Giacomini, D., Schinder, A.F., Avila, J., Llorens-Martin, M., 2019. Activity-Dependent Reconnection of Adult-Born Dentate Granule Cells in a Mouse Model of Frontotemporal Dementia. J. Neurosci. 39, 5794–5815.

Terreros-Roncal, J., Moreno-Jimenez, E.P., Flor-Garcia, M., Rodriguez-Moreno, C.B., Trinchero, M.F., Cafini, F., Rabano, A., Llorens-Martin, M., 2021. Impact of neurodegenerative diseases on human adult hippocampal neurogenesis. Science 374, 1106–1113.

Terreros-Roncal, J., Flor-Garcia, M., Moreno-Jimenez, E.P., Rodriguez-Moreno, C.B., Marquez-Valadez, B., Gallardo-Caballero, M., Rabano, A., Llorens-Martin, M., 2022. Methods to study adult hippocampal neurogenesis in humans and across the phylogeny. Hippocampus.

Tong, J., Liu, Z.C., Wang, D.X., 2011. Azithromycin acts as an immunomodulatory agent to suppress the expression of TREM-1 in Bacillus pyocyaneus-induced sepsis. Immunol. Lett. 138, 137–143.

Toni, N., Laplagne, D.A., Zhao, C., Lombardi, G., Ribak, C.E., Gage, F.H., Schinder, A.F., 2008. Neurons born in the adult dentate gyrus form functional synapses with target cells. Nat. Neurosci. 11, 901–907.

Vacca, M., Celano, G., Calabrese, F.M., Portincasa, P., Gobbetti, M., De Angelis, M., 2020. The Controversial Role of Human Gut Lachnospiraceae. Microorganisms 8.

Vallee, E., Azoulay-Dupuis, E., Pocidalo, J.J., Bergogne-Berezin, E., 1992. Activity and local delivery of azithromycin in a mouse model of Haemophilus influenzae lung infection. Antimicrob. Agents Chemother. 36, 1412–1417.

Venditto, V.J., Haydar, D., Abdel-Latif, A., Gensel, J.C., Anstead, M.I., Pitts, M.G., Creameans, J., Kopper, T.J., Peng, C., Feola, D.J., 2021. Immunomodulatory Effects of Azithromycin Revisited: Potential Applications to COVID-19. Front. Immunol. 12, 574425.

Wiselka, M.J., Read, R., Finch, R.G., 1996. Response to oral and intravenous azithromycin in a patient with toxoplasma encephalitis and AIDS. J. Infect. 33, 227–229.

Yirmiya, R., 1996. Endotoxin produces a depressive-like episode in rats. Brain Res. 711, 163–174.

Zhang, W., Guo, Y., Cheng, Y., Yao, W., Qian, H., 2023. Neuroprotective effects of polysaccharide from Sparassis crispa on Alzheimer's disease-like mice: Involvement of microbiota-gut-brain axis. Int. J. Biol. Macromol. 225, 974–986.

Zhang, B., Kopper, T.J., Liu, X., Cui, Z., Van Lanen, S.G., Gensel, J.C., 2019. Macrolide derivatives reduce proinflammatory macrophage activation and macrophage-mediated neurotoxicity. CNS Neurosci. Ther. 25, 591–600.

Zhao, C., Teng, E.M., Summers Jr., R.G., Ming, G.L., Gage, F.H., 2006. Distinct morphological stages of dentate granule neuron maturation in the adult mouse hippocampus. J. Neurosci. 26, 3–11.